

Measurement of the Volume Expansion of SiC Refractories Induced by Molten Salt Corrosion

E. de Bilbao^{*1}, P. Prigent¹, C. Mehdi-Souzani³,
M.-L. Bouchetou¹, N. Schmitt^{3, 4}, J. Poirier¹, E. Blond⁵

¹CEMHTI, CNRS UPR3079/Université d'Orléans, 1D avenue de
la Recherche Scientifique, 45071 Orléans, France

²LURPA, ENS Cachan/EA 1385, 61, avenue du Président Wilson, 94235 Cachan, France

³LMT-Cachan, ENS Cachan/CNRS UMR 8535/UMPC, 61,
avenue du Président Wilson, 94235 Cachan, France

⁴Université Paris-Est Créteil, Place du 8 Mai 1945, 93203 Saint-Denis, France

⁵Prisme, Université Orléans, 8 rue Léonard de Vinci, 45072 Orléans, France

received April 22, 2013; received in revised form June 3, 2013; accepted June 11, 2013

Abstract

Corrosion tests of oxide-bonded SiC-based refractory cylinders with molten salts (mainly CaSO_4 , K_2SO_4) were performed at high temperature to enable better understanding of the corrosion mechanisms operating in these materials. Salt pellets were placed on the upper surface of small refractory cylinders. After they had been melted, the corrosive product soaked into the pores of the refractory cylinders and partially corroded the SiC phase. SEMEDS analyses showed that CaSiO_3 was the main new phase formed, growing from SiC aggregates into the pores. The shapes of the initial and corroded cylinders were measured at room temperature using a 3D coordinate measuring machine equipped with a laser-plane sensor. These measurements enabled monitoring of the evolution of the residual radial deformation versus the depth from the surface in contact with the salt pellets, and consequently the characterisation of the local volume expansion induced by the phase change. Coupling SEM-EDS analyses with 3D digitising revealed the link between the corrosion product and the volume expansion.

Keywords: Corrosion, SiC, refractories, volume expansion

I. Introduction

The degradation of refractory linings results from the complex interactions between coupled thermo-chemo-mechanical phenomena^{1,2}. Thus, analysing both the thermo-chemical and the thermo-mechanical degradation mechanisms is an ongoing challenge in better understanding the damage and predicting the lifetime of refractory linings.

The corrosion process of SiC-based refractory material is driven by the reactive transport of corrosive agents into the material^{3–5}. In addition to oxidation by steam^{6–9}, corrosion involves a complex series of chemical reactions with molten salts or liquid slag present in a given matrix. In some cases, chemical reactions lead to volume expansion and swelling of the refractory material.

In general, the volume expansion due to corrosion combined with thermo-mechanical loading leads to stresses within refractory parts and therefore damage^{1,10,11} (Fig. 2). Hence, the swelling induced by corrosion plays a key role in the lifetime of refractory materials. These coupled phenomena are not yet understood and studying both the thermo-chemical and thermo-mechanical behaviour is

an ongoing challenge. The objectives of this study were:

- To develop a corrosion test on laboratory scale to study the role of new phases in inducing strain. Hence, the test presented in this paper was inspired by an industrial case of corrosion of SiC-based refractory by molten salts and consisted of analysing the formed phases with SEM-EDS and measuring the variation in the shape of the tested samples by means of 3D digitising. Section 2 describes the corrosion process.
- To relate the non-uniform chemical corrosion of refractory materials by molten salts to the observed non-uniform volume expansion. Section 3 presents the corrosion test associated with the volume expansion measurement. The results are presented and discussed in section 4.

II. Corrosion Mechanisms

The corrosion of oxide-bonded SiC-based refractory materials by molten salts has been studied^{10,12}. In this case, the corrosive species originate from gases and flying ashes that flow mainly into the pores of the matrix. They then condense at lower temperatures owing to the thermal gradient that generally exists through the thickness of a lining. The condensed species fill the porous network and

* Corresponding author: emmanuel.de-bilbao@univ-orleans.fr

react either directly with SiC grains or with the matrix. They eventually dissolve the matrix, thereby reaching the SiC grains.

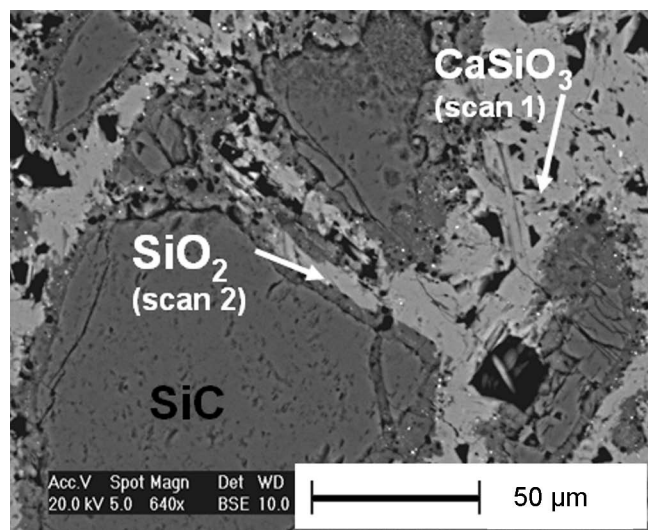


Fig. 1: Example of corroded and swelled SiC-based refractory tile.

Table 1: EDS analyses of Fig. 1.

Elements	Scan 1 (wt%)	Scan 2 (wt%)
O	49.6	41.3
Si	22.2	24.2
S		0.9
K		0.7
Ca	28.0	32.5

It is clear that the process depends on at least the composition of the refractory material, the molten salts and the temperature. The refractory materials studied were composed of SiC (90 wt%), with an alumina-silicate matrix, the corrosive agents were calcium sulphate and alkali compounds (CaSO_4 , K_2SO_4 , Na_2SO_4 and HCl , NaCl) and the processing temperature was 860 °C. Experiments and thermochemical simulations performed at equilibrium using FactSage© thermodynamic software¹³ enabled the proposition of a scheme for the corrosion process¹⁴. The corrosion by molten salts was described by two main mechanisms. The first mechanism consists in the formation of para-wollastonite (CaSiO_3). Calcium sulphate and alkali compounds (CaSO_4 , K_2SO_4 , Na_2SO_4 and HCl , NaCl) condense as molten salts react with silica present in the matrix and SiC grains as well. The SiO_3^{2-} ions then react with Ca^{2+} cations from the dissociation of calcium sulphate at high temperature to form CaSiO_3 . The second mechanism consists first in the condensation of alkali sulphate species in the pores of the refractory material. Na and K present in the molten salts penetrate the matrix as network modifiers. The presence of alkalis leads to the formation of cristobalite around the SiC grains and in the matrix at lower temperature¹⁵. The high potassium content in the alumina-silica matrix can lead to the formation of microcline (KAlSi_3O_8). Scanning electron microscopy (SEM) (Fig. 1) and energy-dispersive X-ray spectroscopy

(EDS) (Table 1) performed on an oxide-bonded SiC refractory materials corroded by salts confirmed the formation of CaSiO_3 (scan 2) in the matrix and SiO_2 (scan 1) around a SiC grain.

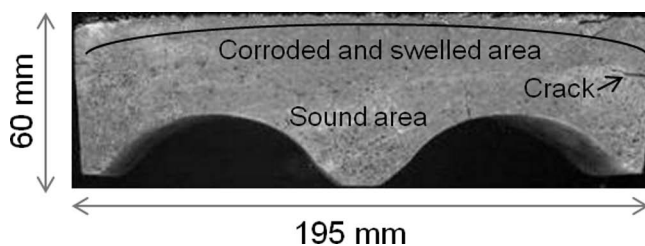


Fig. 2: Example of microstructure of an oxide-bonded SiC refractory material corroded by salts.

The formation of para-wollastonite and cristobalite is accompanied by volume expansion. After filling the initial voids the corrosion product – in the solid state – pushes the walls of the solid phases, inducing macroscopic swelling. In addition, the formed microcline is a viscous phase that can promote the strain induced by the para-wollastonite and cristobalite. Tests have therefore been performed on lab scale in order to better understand and quantify the relationship between corrosion and volume expansion.

III. Materials and Techniques

The macroscopic swelling induced by corrosion was estimated by measuring the variation in the shape of a refractory sample before and after the corrosion test. The sample was weighed before and after testing. The refractory was composed of SiC (90 wt%) with an alumina-silicate matrix. The properties of the sample are presented in Table 2. Cylindrical samples ($\varnothing 30 \text{ mm} \times \text{H} 30 \text{ mm}$) were prepared by means of diamond core drilling using water as a lubricant. The corrosion test consisted of placing the cylindrical samples into a furnace and heating them to 860 °C in air (Fig. 3). After a one-hour dwell, one or several corrosive pellets were placed on the top of the samples, and the samples were held under these conditions for 100 hours. The mass of each pellet was 3.5 g. When several pellets were used for one cylinder, they were placed on the surface successively every half hour. Then, the samples were freely cooled. The corrosive agents, pressed into tablets, were composed of sulphate species (CaSO_4 , K_2SO_4 , Na_2SO_4) and alkali chlorides were added to decrease the liquidus temperature¹⁶ (Table 3). Preliminary tests performed on a cubic sample ($20 \times 20 \times 20 \text{ mm}^3$, 21 g) showed that it was fully impregnated with three pellets (10.5 g) while the mass of the sample increased by only 11 %. The difference was due to the vaporisation of some species. In addition, a reference sample was subjected to the same heat treatment but without corrosive pellets to compare the results. After the shapes of the corroded samples had been measured, the samples were cut along the main axis and prepared for analyses. The microstructure was studied by means of SEM, and species contents were determined with EDS (FEI ESEM XL40).

The residual deformation of the cylinders at room temperature was characterised by measuring the variation in the macroscopic volume of thin layers located at several

distances from the surface in contact with the pellets. Because small residual deformation was expected, typically from 0.1 to 1 %, the residual radial expansion of the cylindrical samples, measuring 30 mm in diameter, ranged from 0.03 to 0.3 mm. Consequently, both the resolution and measurement uncertainty of the measurement device used must be less than or equal to one micrometre.

Table 2: Characteristics of studied refractory material.

Composition (wt%)		Physical properties	
SiC	90	Bulk density	2650 kg/m ³
SiO ₂	8	Open porosity	15 %
Al ₂ O ₃	2.5	Cold crushing strength	110 MPa
Fe ₂ O ₃	0.2	Thermal conductivity	13 W/mK at 1100 °C

Table 3: Chemical composition of the corrosive agents used for the test.

Species	wt%
CaSO ₄	53.6
K ₂ SO ₄	27.4
Na ₂ SO ₄	5.6
KCl	8.8
NaCl	4.6

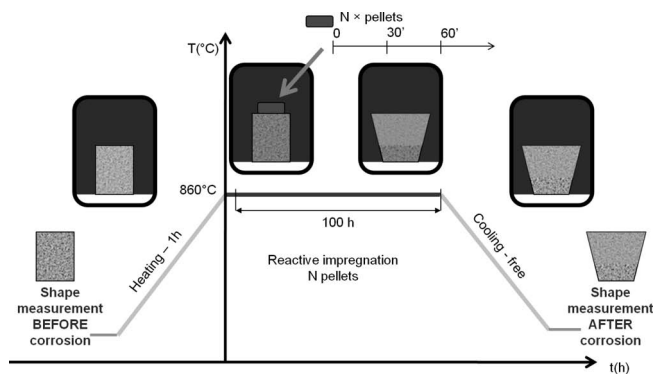


Fig. 3: Corrosion test cycle.

The experimental measurement was performed in two main steps: i) 3D digitising of the samples and ii) post-processing of the cloud of points to compute the volume variation. The shapes of the samples were accurately measured before and after the corrosion test with a 3D coordinate measuring machine (CMM), Renault Automation 13–8-6. This device is equipped with a laser-plane sensor (Fig. 4) mounted on a motorised indexing head (Renishaw PH10), enabling the sensor to be oriented along repeatable discrete orientations that can be achieved through two rotations. When the orientation correspondence is defined, the sensor can be moved according to the three motorised translation axes of the CMM. Such a configuration increases

the sensor's accessible space. The contactless sensor used (Kreon-Zephyr KZ25) consists of a laser-plane beam that is projected onto the part to be measured. The intersection curve between the part surface and the laser plane is observed in the 2D space of a CCD camera. Based on triangulation and pinhole modelling, the relationship between the 2D data acquired and the 3D coordinates of points belonging to the object surface can be determined. To scan an entire surface, the sensor is moved over the digitised part. The sensor is characterised by a scanning window, generally called the *field of view* (FOV), corresponding to the area of the scanning plane that is visible by the camera. Only the points of intersection between the laser beam and the part surface belonging to the FOV are collected and define the digitised line. The position and orientation of the sensor compared to the measuring surface greatly affects the quality of the digitised data¹⁷. To accurately digitise a surface, the setting of the FOV with respect to the part surface must be optimal. In this study, an automatic digitising process planning algorithm¹⁸ was used.

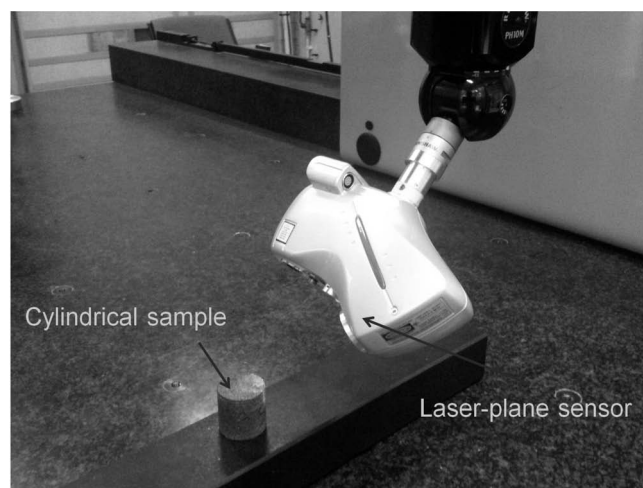


Fig. 4: The laser-plane sensor mounted on the 3D coordinates measurement machine (Renault Automation 13–8-6 motorised CMM) used to measure the dimensions of the samples before and after corrosion testing. The sample is about approximately 30 mm in diameter.

Using a contactless laser-plane sensor enabled the collection of a very large cloud of points per sample – typically up to 800 000 points – and post-processing the set of points allowed the assessment of the volume change along the axis of the cylindrical samples. The shape of each theoretically cylindrical sample was actually complex because it became even more irregular after corrosion. Therefore, the volume of the samples was estimated by describing the complex rough surface as a sum of elementary surfaces. In the first stage, a virtual cylinder was associated with the set of points, with the radius and the axis computed using the least-squares method (Fig. 5a). The overall region containing the whole set of points was then split into successive sub-regions, i.e. slices, delimited by planes perpendicular to the cylinder axis that could either be overlapped or not. The carving of the cloud of points was driven by two parameters: i) the thickness of the slices (denoted “*t*”) and the distance between two successive slices (denoted “*s*”). The points belonging to each slice were projected onto the lower plane

delimiting the slice, and a circle was derived with the least-squares method (Fig. 5b). Assuming axisymmetric deformation, the variation in the mean radius before and after corrosion was then computed. Comparing the circularity of the set of points before and after corrosion allowed for the verification of the assumption of axisymmetry. Finally, the volume of each slice was computed using the radius and thickness of the circle derived, and the total sample volume was determined by means of summation.

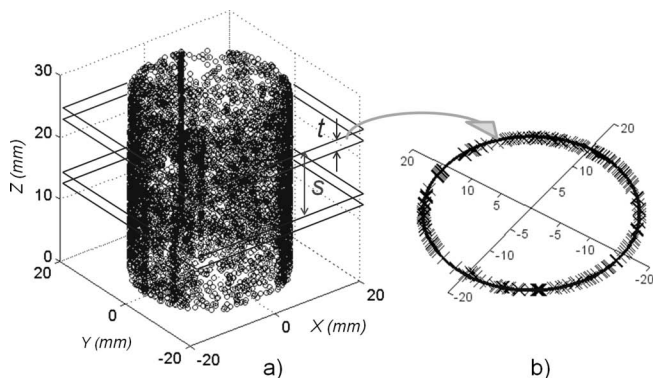


Fig. 5: Scan of sample B with laser-plane sensor. Only 1 point in 100 is plotted in the illustration. a) Cloud of points of the cylindrical part. b) Projected points of slice located at $Z = 27$ mm

IV. Results and Discussion

The conditions of the corrosion tests are summarised in Table 4. Samples A and B were submitted to the action of corrosive pellets, while the reference sample C, subjected to the same heat treatment, was not corroded. Partial impregnation and a gradient in the corrosive species content were expected in the corroded samples.

Table 4: Experiment protocol.

Sample	A	B	C
State	Corroded		Non-corroded
Geometry	Cylindrical $\varnothing 30$ mm \times H30 mm		
Temperature ($^{\circ}\text{C}$)	870		
Duration (hours)	100		
Pellets (nb)/(g)	2 / 7		0

Table 5: Weight and volume changes.

Sample	$\Delta W/W$ (%)	$\Delta V/V$ (%)
A	2.76	0.54
B	2.72	0.60
C	-0.05	-

For the reference sample C, the defined thermal cycle led to a small mass loss and imperceptible variation in geometry (Table 5). For the corroded samples A and B, significant changes in weight were measured; the increase in mass was

due to the action of corrosive species, but did not correspond to the total mass of the tablets because some species vaporised (Cl, Na, S).

The variations in the radius, R , and standard deviation, S , are plotted along the axis measured for sample B in Fig. 6. The radius was computed using the circle optimised with the least-squares method; it represents the mean profile of the sample. The standard deviation was derived from the residuals; the standard deviation indicates the representativeness of the mean profile. The radius and standard deviation were computed for non-corroded (a and b indices) and corroded (d and e indices) states using two sets of values of t and s (a, d and b, e) to compare the influence of the computation parameters (t and s) on the curves $R-a$, $S-a$ and $R-b$, $S-b$ corresponding to the non-corroded state, while $R-d$ and $R-e$ correspond to the corroded state (Table 6). The curve $R-a$ was computed with $t = s = 0.5$ mm, considering that the slices were contiguous. The radius ranges from 14.80 to 15.02 mm. This interval is in agreement with the coring capability. The irregularities in the radius observed for the non-corroded samples tallied with those observed for the corroded sample. In addition, irregularities in the standard deviation are in agreement. They then may be due to the roughness defects generated on the surfaces by coring. For a distance coordinate Z , the volume change between the non-corroded and corroded states was defined as the difference in the volumes of the slices corresponding to the same coordinates and the volume derived from the thickness and the square of the radius of the slices. The thickness, t , and step, s , were defined to smooth the curve and to limit the propagation of the irregularities of the radius through the volume assessment. Increasing the step smoothed the curve but decreased the resolution. Increasing the thickness smoothed the curve more weakly without decreasing the resolution. Several attempts finally led to the selection of $t = 3$ mm and $s = 2$ mm as a good compromise. This setting constituted a low-pass filter stopping roughness defects ($R-a/R-b$, $R-d/R-e$ and $S-a/S-b$) that did not distort the change in radius between the non-corroded and corroded samples ($R-a/R-d$ compared to $R-b/R-e$).

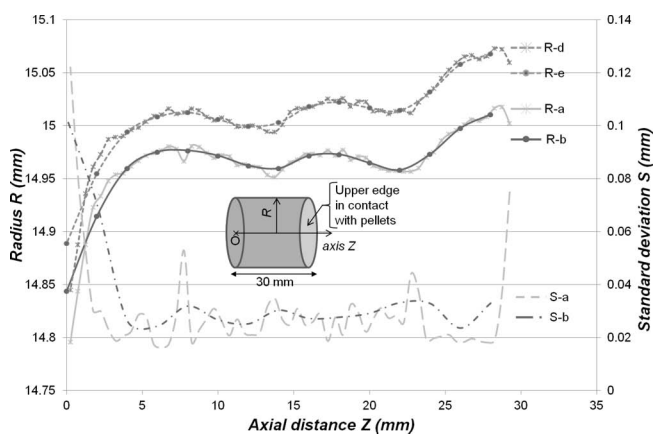


Fig. 6: Radius evaluation depending on post-processing parameters for sample B.

Table 6: Comparison of post-processing conditions.

Sample	Post-processing parameters	
	t=0.5 s=0.5	t=3 s=2
Non-corroded	R-a, S-a	R-b, S-b
Corroded	R-d, S-d	R-e, S-e

The volume of each slice V_s was computed from the thickness e_s and the radius R_s , and the volume change $\Delta V_s/V_s$ was then derived and plotted along the axis (Fig. 7). The volume expansion of the slices was not uniform. The expansion ranged from 0.30 to 0.70 % (average 0.54 %) and from 0.45 to 0.80 % (average 0.60 %) for samples *A* and *B*, respectively. Both curves are non-linear with *Z*. However, for sample *A*, a quite linear expansion ($R^2 = 0.97$) is observed from the bottom to 20 mm, with a saturation of the volume change in the upper part. For sample *B*, the variation in the volume does not show a specific tendency in the lower part, and a linear change ($R^2 = 0.99$) is observed from 8 to 24 mm. It is worth reiterating that the curves were smoother to filter out erroneous measurements. However, the irregularities in the changes may have also been due to the heterogeneities of the materials which induced both heterogeneous strain and reactive impregnation. Hence, the most relevant analysis is that of the constant gradient of the volume change.

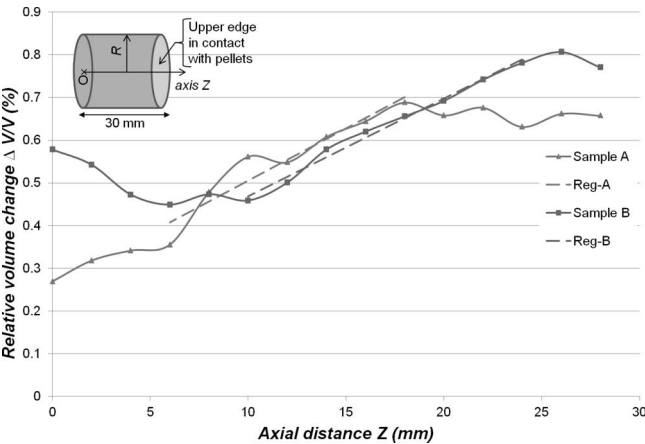


Fig. 7: Relative volume change along the impregnation direction for samples *A* and *B*.

SEM-EDS analyses were performed on the samples. The results show that the corrosion tests produced CaSiO_3 as expected. The microstructure of sample *B* was studied with SEM, and the species contents were determined by means of EDS before and after the corrosion test in detail. Fig. 8 shows the microstructure of an area located in the plane parallel to the upper face 5 mm from the top. Needles of para-wollastonite were formed around the SiC grains and in the matrix. The chemical composition of the dense phase formed in the matrix was different from that before corrosion: the Si content was higher, and traces of Na, K, S were detected at lower concentration. Potassium partially produced microcline, with alumina and silica composing the initial matrix. Fig. 9 shows the evolution of potassium and calcium contents along the *Z* axis. Potassium intruded into the matrix of nearly the entire cylinder, forming a viscous microcline phase. Beyond $Z = 20$ mm, the

potassium content increases and reaches a peak at 25 mm. The following decrease may have been due to vaporisation. From the bottom of the sample up to $Z = 20$ mm, the Ca content is not significant whereas it does not exist in the non-corroded material. Meanwhile, the Ca content rises up to 3.8 % at the top. With EDS analyses, only species can be identified, and one cannot ensure that all of the calcium and potassium completely formed the observed para-wollastonite and microcline phases. However, the evaluated species contents were close to those found in para-wollastonite. Moreover, high-temperature X-ray diffraction performed on sample powders showed that para-wollastonite formed in less than 15 minutes¹². Thus, it can be assumed that calcium completely formed the expansive phase in 100 hours.

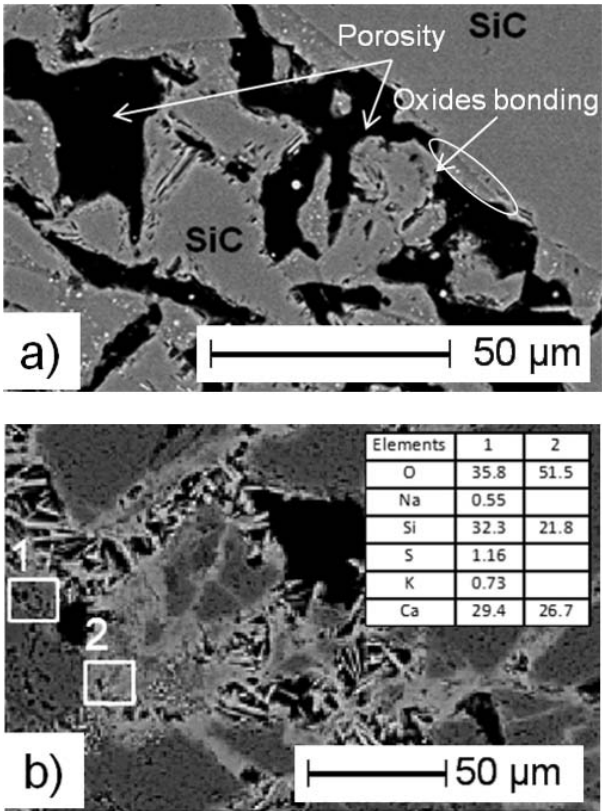


Fig. 8: Microstructure of oxide-bonded SiC-based refractory sample before (a) and after (b) corrosion by molten salts (Sample *B*, location $Z = 5$ mm).

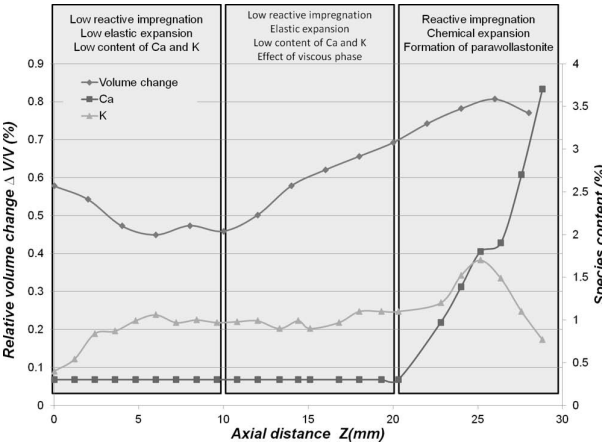


Fig. 9: Volume variation along axis of corroded sample *B* as a function of species content.

Finally, plotting the contents of both species versus the relative change in volume along the sample axis makes it possible to correlate the swelling to the corrosion, particularly that due to the formation of para-wollastonite and microcline. With regard to the three curves, sample *B* can be split into three regions. Beginning from the top, the upper part (30–20 mm) is well impregnated and the formation of para-wollastonite has induced chemical strain and volume change. In the middle part (20–10 mm), the low content of potassium did not likely induce chemical strain but the viscous phase at the considered temperature, i.e. microcline formed due to potassium, allows for elastic deformation induced by irreversible strain within the upper part. Finally, in the bottom part (10–0 mm), the low volume variation is likely to be induced by the strain field of the area above due to the potassium.

V. Conclusions

The corrosion of oxide-bonded SiC-based refractory materials by molten salts has been studied. The results clearly show that the corrosion mechanism is not homogeneous in the volume of the corroded sample. Gradients of chemical species were consistently observed although the temperature in the samples was uniform, making it difficult to describe the chemical corrosion processes in detail. Consequently, the associated physical properties, such as the chemical swelling, are also non-uniform and therefore not easy to measure using the conventional method.

The volume expansion owing to the chemical reactions was assessed using an innovative measurement technique with which the shapes of the samples were determined using a 3D CMM equipped with a laser plane-sensor. Measuring the sample shapes before and after corrosion testing made it possible to accurately compute local volume changes along the direction of corrosive impregnation. Finally, combining both micro-structural analysis and the accurate local measurement of the volume changes due to corrosion allowed for the link between local volume expansion and corrosion to be established. In some cases, the observed swelling can be as large as the thermal strain and can induce cracks on the microscopic scale. Depending on the thermo-mechanical loading, cracks can also appear on macroscopic scale within the refractory parts owing to the volume expansion induced by corrosion. The developed approach is thus promising, as it improves our knowledge of the coupling between phase changes during corrosion and one of the most important physical consequences, the “chemical” change in volume which plays an important role in the service lifetime of refractory parts.

References

- ¹ Blond, E., Schmitt, N., Hild, F., Blumenfeld, P., Poirier, J.: Effect of slag impregnation on thermal degradations in refractories, *J. Am. Ceram. Soc.*, **90**, (1), 154–162, (2007).
- ² Lee, W.E., Moore, R.E.: Evolution of *in situ* refractories in the 20th century, *J. Am. Ceram. Soc.*, **81**, (6), 1385–1410, (1998).
- ³ Lee, W.E., Zhang, S.: Melt corrosion of oxide and oxide-carbon refractories, *Int. Mater. Rev.*, **44**, (3), 77–104, (1999).
- ⁴ Rezaie, A., Headrick, W.L., Fahrenholtz, W.G., Moore, R.E., Velez, M., Davis, W.A.: Interaction of refractories and alkaline containing corrodants, *Refractories Applications and News*, **9**, (5), 26–31, (2004).
- ⁵ Rau, A.W.: CFB refractory improvements for biomass co-firing, *Power Eng.*, **114**, (7), 36–44, (2010).
- ⁶ Vaughn, W.L., Maahs, H.G.: Active-to-passive transition in the oxidation of silicon carbide and silicon nitride in air, *J. Am. Ceram. Soc.*, **73**, (6), 1540–1543, (1990).
- ⁷ Wang, G.X., Lu, G.Q., Pei, B., Yu, A.B.: Oxidation mechanism of Si₃N₄-bonded SiC ceramics by CO, CO₂ and steam, *J. Mater. Sci.*, **33**, (5), 1309–1317, (1998).
- ⁸ More, K.L., Tortorelli, P.F., Ferber, M.K., Keiser, J.R.: Observations of accelerated silicon carbide recession by oxidation at high water-vapor pressures, *J. Am. Ceram. Soc.*, **83**, (1), 211–213, (2000).
- ⁹ Gallet-Doncieux, A., Bahloul, O., Gault, C., Huger, M., Chotard, T.: Investigations of SiC aggregates oxidation: Influence on SiC castables refractories life time at high temperature, *J. Eur. Ceram. Soc.*, **32**, (4), 737–743, (2012).
- ¹⁰ Prigent, P., Bouchetou, M.-L., Poirier, J., Brossard, J.-M.: Study of the corrosion mechanisms of SiC refractory lining in municipal solid waste-to-energy facilities, in: Proceedings of Unitec’ 2009, Salvador (Brazil), 2009.
- ¹¹ Tonnensen, T., Telle, R.: Refractory corrosion in industrial waste incineration processes, *Refractories WORLDFORUM*, **1**, (1), 71–76, (2009).
- ¹² Prigent, P., Bouchetou, M.-L., Poirier, J.: Corrosion of SiC based refractories by molten salts in municipal solid waste-to-energy facilities, in: Proceedings of conference of metallurgists, Vancouver (Canada), 2010.
- ¹³ Bale, C.W., Chartrand, P., Degterov, S.A., Eriksson, G., Hack, K., Ben Mahfoud, R., Melançon, J., Pelton, A.D., Petersen, S.: FactSage thermochemical software and databases, *Calphad*, **26**, (2), 189–228, (2002).
- ¹⁴ Prigent, P., Bouchetou, M.-L., Poirier, J., de Bilbao, J., Blond, E.: Corrosion of oxide bonded silicon carbide refractories by molten salts in solid waste-to-energy facilities, *Ceram. Int.*, **38**, (7), 5643–5649, (2012).
- ¹⁵ Tomita, K., Kawano, M.: Effect of cations on crystallization of amorphous silica. II, *Kagoshima Daigaku Rigakubu Kiyo. Chigaku seibutsugaku*, **26**, 1–16, (1993).
- ¹⁶ Akopov, E.K., Bergman, A.G.: Decomposition of the solid solutions in the reciprocal system of the chlorides and sulfates of sodium and potassium, *Zhur. Neorg. Khim.*, **4**, 1653–1656, (1959).
- ¹⁷ Mehdi-Souzani, C., Lartigue, C.: Contact less laser-plane sensor assessment : Toward a quality measurement, in: Proceedings of IDMME-virtual concept 2008, Beijing (China), 2008.
- ¹⁸ Mehdi-Souzani, C., Thiebaut, F., Lartigue, C.: Scan planning strategy for a general digitized surface, *J. Comput. Inf. Sci. Eng.*, **6**, (4), 331–339, (2006).